

From Saliency to DINO: Saliency-guided Vision Transformer for Few-shot Keypoint Detection

Changsheng Lu¹, Hao Zhu¹, Piotr Koniusz^{2,1}

¹The Australian National University ²Data61/CSIRO

{ChangshengLuu, allenhaozhu}@gmail.com, Piotr.Koniusz@data61.csiro.au

Abstract

Unlike current deep keypoint detectors that are trained to recognize limited number of body parts, few-shot keypoint detection (FSKD) attempts to localize any keypoints, including novel or base keypoints, depending on the reference samples. FSKD requires the semantically meaningful relations for keypoint similarity learning to overcome the ubiquitous noise and ambiguous local patterns. One rescue comes with vision transformer (ViT) as it captures long-range relations well. However, ViT may model irrelevant features outside of the region of interest due to the global attention matrix, thus degrading similarity learning between support and query features. In this paper, we present a novel saliency-guided vision transformer, dubbed SalViT, for few-shot keypoint detection. Our SalViT enjoys a uniquely designed masked self-attention and a morphology learner, where the former introduces saliency map as a soft mask to constrain the self-attention on foregrounds, while the latter leverages the so-called power normalization to adjust morphology of saliency map, realizing “dynamically changing receptive field”. Moreover, as saliency detectors add computations, we show that attentive masks of DINO transformer can replace saliency. On top of SalViT, we also investigate i) transductive FSKD that enhances keypoint representations with unlabelled data and ii) FSKD under occlusions. We show that our model performs well on five public datasets and achieves $\sim 10\%$ PCK higher than the normally trained model under severe occlusions.

1. Introduction

The deep fully-supervised learning relies on large amounts of labelled data for training and cannot generalize to novel classes well. In contrast, humans learn new concepts from few samples, which motivates the need for few-shot learning (FSL) [41] in various tasks such as image classification [34, 18, 33, 38, 23], object detection [22, 14, 40, 49], segmentation [26, 24], and keypoint de-

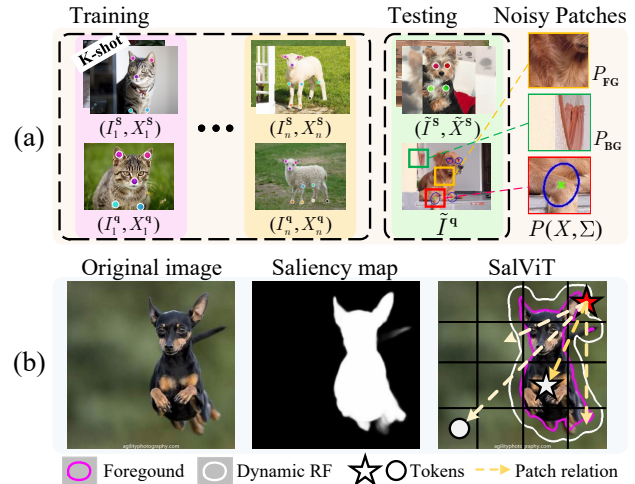


Figure 1. Few-shot keypoint detection (FSKD) and patch relations guided by saliency. (a) We train and test FSKD model via episodes, each containing a support image I^s , support keypoints X^s , and the query image I^q . The goal is to infer the keypoints X in I^q that correspond to X^s . P_{FG} and P_{BG} show the noisy foreground and background patches. $P(X, \Sigma)$ shows the predicted keypoint X with uncertainty Σ by our model (best viewed in zoom); (b) The saliency map indicates the foreground patches. Our SalViT can enhance the relation learning for the pairwise salient patches (or “tokens”) while suppressing non-salient pairs.

tection [29, 16]. The emerging few-shot keypoint detection (FSKD) localizes keypoints in query images given one or a few support images with keypoint annotations (Fig. 1(a)). The hardest FSKD setting (which we use among other settings) is that both the base keypoints/species in training are disjoint with the novel keypoints/species in testing, which is challenging due to the large domain shifts.

Compared to general FSL, FSKD shares two common challenges: 1) generalization to unseen classes; 2) low number of samples. Though seminal works [38, 33, 34] address some of such issues, FSKD faces additional challenges. Firstly, keypoints represent semantic local regions that are smaller/harder to detect than holistic objects (*c.f.* FSOD [14]). Secondly, as shown in Fig. 1(a), the noisy patches from foreground and background will affect FSKD. More-

over, the predicted and groundtruth keypoints inherently exhibit ambiguity in location. While modeling both localization and semantic uncertainty [29] helps, the interference from ambiguous local patterns is hard to solve. As each keypoint has close semantic and spatial relationships with other foreground patches, *e.g.* left-eye lying left to right-eye and above on shoulder, such relations require “context modeling”. Thus, we argue that the long-range foreground relations may improve FSKD.

Vision transformer (ViT) [13, 30] is a natural choice to capture such long-range relations. However, the global receptive field of self-attention (SA) in ViT leads to costly computations, and introduces irrelevant features outside of foregrounds [43]. Thus, we propose to use saliency maps, as they are convenient priors locating foreground objects that could help SA focus on foregrounds (Fig. 1(b)) and ignore backgrounds. Interestingly, we also observe high similarity of attentive regions of DINO [7] with saliency, which enables the use of DINO as both backbone and “saliency” detector to cut the number of parameters/computations.

In this paper, we present a saliency-guided vision transformer (SalViT) for few-shot keypoint detection (FSKD). Our SalViT is a plug-and-play module within encoder, which processes the raw support and query features individually, guided by saliency maps of support and query images. SalViT produces informative features relevant for support keypoint prototype (SKP) building, similarity learning, and query keypoint localization. Moreover, since the low-shot samples are insufficient to provide representative SKPs (*e.g.*, 1-shot setting), we propose a transductive FSKD setting to enrich SKPs with unlabeled data. Finally, to improve robustness of our FSKD, we investigate masking and alignment (MAA) strategies, and probe the FSKD performance under occlusion setting.

Our contributions are summarized as follows:

- i. We present a new variant of ViT called as saliency-guided vision transformer (SalViT), which has two key components: masked self-attention (M-SA) and morphology learner (ML). M-SA captures distant relation between salient patches while ML adapts saliency and provides “dynamic receptive field” to exploit useful information in the proximity of foregrounds.
- ii. We propose the pipeline of few-shot keypoint detection (FSKD) with SalViT. Moreover, a transductive extension of FSKD is explored.
- iii. We propose a simple masking and alignment (MAA) strategy that helps detect occluded keypoints.

Experiments on *five* datasets show the superiority of the proposed SalViT-based FSKD model and the occlusion setting indicates that the simple MAA endows our model with stronger occlusion handling capability.

2. Related Work

Few-shot Learning (FSL): Family of deep metric FSL models encourages the inter-class distance to be larger than the intra-class distance [23, 38, 33, 34]. Vinyals *et al.* [38] formalize N -way K -shot protocol with episodes. Snell *et al.* [33] propose ProtoNet with centroids representing classes. Sung *et al.* [34] propose a relation head to measure similarity. Other works emphasize adaptation and optimization (*e.g.* MAML [15]) and data hallucination [46].

Vision Transformers: Transformers [37] are popular in sequential modeling/natural language processing (*e.g.*, BERT [12] and GPT-3 [3]), and computer vision [32]. Vision Transformer (ViT) [13] has inspired data efficient DeiT [35], self-supervised DINO [7], and CrossViT [8], *etc.* Although ViTs often outperform CNNs on classification problems, they do not provide multi-scale features for dense prediction tasks. Thus, other general-purpose architectures such as Swin-T [28] and Twins [10] were proposed.

Masked Attention: Attention mechanisms include *self-attention* (SA) and *cross-attention* (CA) [37, 21]. SA is crucial in ViT modeling but its computation is high as SA operates globally. To remedy this, Swin-T [28] applies SA within the masks of local windows. Twins [10] perform locally-grouped self-attention and then global sub-sampled attention. Unlike Swin-T and Twins using regular windows (*i.e.*, rectangle) with hard masking, we use saliency map to obtain “soft masks” of foreground shapes, serving as the foreground attention. The masked attention is widely used [4, 9, 25] for invalid-token masking, self-supervised training [19, 44], image inpainting [25], *etc.* However, the masked self-attention (M-SA) in our SalViT is uniquely crafted for FSKD. Our M-SA cooperates with a morphology learner which provides “dynamic receptive field” for adaptation on top of detected salient regions.

3. Method

3.1. Preliminary

Vanilla ViT [13]. For a sequence of n tokens of d dimensional feature vectors in $\mathbf{X} \in \mathbb{R}^{n \times d}$, \mathbf{X} forms \mathbf{Q} , \mathbf{K} , $\mathbf{V} \in \mathbb{R}^{n \times d}$ (*i.e.* query, key, and value) by linear projections

$$\mathbf{Q} = \mathbf{X}\mathbf{W}_q, \quad \mathbf{K} = \mathbf{X}\mathbf{W}_k, \quad \mathbf{V} = \mathbf{X}\mathbf{W}_v, \quad (1)$$

where \mathbf{W}_q , \mathbf{W}_k , and \mathbf{W}_v are projection matrices. The self-attention (SA) is applied to learn relations between tokens

$$A_{i,j} = \gamma(\phi(\mathbf{Q}_{i,:}, \mathbf{K}_{j,:})), \quad \tilde{\mathbf{V}} = \mathbf{A}\mathbf{V}, \quad \mathbf{Z} = \tilde{\mathbf{V}}\mathbf{W}_o, \quad (2)$$

where $\gamma(\cdot)$ is a non-linear function and $\phi(\cdot)$ is a similarity function, the two together yielding attention $\mathbf{A} \in \mathbb{R}^{n \times n}$. \mathbf{W}_o is a projection matrix, and \mathbf{Z} is the output of SA. Functions (γ, ϕ) can be the *scaled dot-product based softmax SA*, *i.e.*, $\gamma(\cdot) = \text{softmax}(\cdot)$, $\phi(\mathbf{Q}_{i,:}, \mathbf{K}_{j,:}) = \mathbf{Q}_{i,:} \mathbf{K}_{j,:}^T / (\beta\sqrt{d})$,

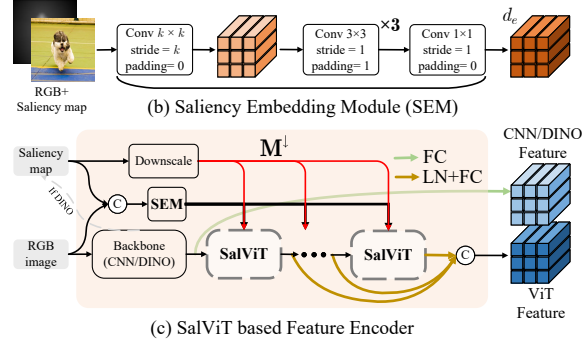
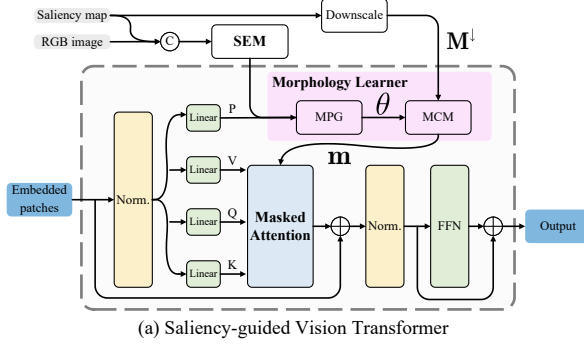


Figure 2. Model overview. (a) The architecture of saliency-guided vision transformer (SalViT); (b) details of semantic embedding module (SEM); (c) SalViT-based feature encoder \mathcal{E} for FSKD.

Table 1. Statistic mean-IoU of each saliency prior to that of SCRNN.

mIoUs	MNL	DINO	RBD	WScribble
Animal Dataset [5]	0.698	0.576	0.343	0.757
AwA Dataset [1]	0.697	0.575	0.412	0.753

or *Gaussian kernel based RBF SA*, i.e., $\gamma(\cdot) = \exp(\cdot)$, $\phi(\mathbf{Q}_{i,:}, \mathbf{K}_{j,:}) = -\|\mathbf{Q}_{i,:} - \mathbf{K}_{j,:}\| / (2\beta\sqrt{d})$. To accelerate computation, \mathbf{Q} , \mathbf{K} , \mathbf{V} are split into multiple sub-matrices in channel dimension and computed via multi-head self-attention (MHSA). Finally, a feedforward network (FFN) comprised by two linear layers with GELU activation is used. With the layer normalization (LN) and skip connection, a basic ViT block becomes

$$\mathbf{Z}'_l = \text{MHSA}(\text{LN}(\mathbf{Z}_{l-1})) + \mathbf{Z}_{l-1}, \quad \mathbf{Z}_l = \text{FFN}(\text{LN}(\mathbf{Z}'_l)) + \mathbf{Z}'_l, \quad (3)$$

where \mathbf{Z}_l is the output of l -th ViT. Based on vanilla ViT, we will build our SalViT in next section.

3.2. Saliency-guided Vision Transformer

Our SalViT is shown in Fig. 2(a), which includes masked self-attention (M-SA), morphology learner (ML), and saliency embedding module (SEM), in addition to the components of vanilla ViT. The ML takes patch features \mathbf{P} and saliency embeddings produced by SEM as input, and predicts a conditional parameter θ to change the morphology of saliency map, yielding an adapted mask for M-SA. In what follows, we will detail each component of SalViT.

3.2.1 Saliency Map Generation

Visual saliency, relating to human visual attention, is given as a single-channel map with values in $[0, 1]$ range. The conventional saliency detectors (e.g., RBD [51]) are modeled by various handcrafted priors, and underperform on complex scenes. More robust deep saliency detectors include i) unsupervised detectors, e.g. MNL [48]; ii) supervised ones, e.g. SCRNN [42] and WScribble [47]. MNL is robust and it does not use human annotations [48, 46].

We validate the performance of each saliency detector by computing mean IoU to the state-of-the-art SCRNN on

two FSKD datasets (Table 1). Also, inspired by the self-supervised vision transformer DINO [7], and its impressive unsupervised semantic segmentation, we treat the *class token attentiveness* [27, 7] from the pre-trained DINO (ViT-S/16) as another form of ‘‘saliency prior’’. DINO yields over 57% mean IoU: it captures salient regions. Thus, we use unsupervised MNL or DINO for saliency priors in main experiments. We investigate other saliency detectors in Sec. 4.3. With saliency, ViT captures salient patch relations well.

3.2.2 Soft Masked Self-attention

The vanilla SA is given as $A_{i,j} = \gamma(\phi(\mathbf{Q}_{i,:}, \mathbf{K}_{j,:}))$ (Eq. 2). We take downsampled saliency map \mathbf{M}^\downarrow flattened as $\mathbf{m} \in \mathbb{R}^n$ (n is the number of tokens) to incorporate saliency into SA as $A_{i,j} = \gamma(\psi(\mathbf{Q}_{i,:}, \mathbf{K}_{j,:}, m_i, m_j))$, where m_i, m_j are the saliency of i -th and j -th patches, respectively. Intuitively, the attention should be encouraged to attend patch relations on target object given \mathbf{m} . We define (γ, ψ) as

$$\gamma(\psi(\mathbf{Q}_{i,:}, \mathbf{K}_{j,:}, m_i, m_j)) = \begin{cases} \gamma(\phi(\mathbf{Q}_{i,:}, \mathbf{K}_{j,:})) & i, j \in \mathcal{S}_+ \\ 0 & i \in \mathcal{S}_+, j \in \mathcal{S}_- \\ \delta(i - j) & i \in \mathcal{S}_- \end{cases} \quad (4)$$

where $\mathcal{S}_+ \equiv \{i : m_i \geq 0.5\}$ (or $\mathcal{S}_- \equiv \{i : m_i < 0.5\}$) stands for the index set of foreground (or background) patches and $\delta(i - j)$ is 1 if $i = j$, 0 otherwise. Our choice of (γ, ψ) means that the relation of the pair of foreground patches is learned, foreground-background pair is inactive, and background patch only focuses self-information. However, such hard masking is inapplicable in real scenario as one patch grid may mix both foreground and background information. Thus, we propose a soft-masked self-attention (M-SA). Firstly, we define a so-called saliency interaction matrix (SIM), $\bar{\mathbf{M}} \in \mathbb{R}^{n \times n}$, which represents the saliency degree of paired patches. We can use 1) dot-product, i.e. $\bar{\mathbf{M}} = \mathbf{m}\mathbf{m}^\top$; 2) harmonic mean, i.e. $\bar{\mathbf{M}} = 2\mathbf{m}\mathbf{m}^\top / (\mathbf{m}\mathbf{1}^\top + \mathbf{1}\mathbf{m}^\top + \epsilon)$ ($\epsilon \rightarrow 0$); and 3) arithmetic mean, i.e. $\bar{\mathbf{M}} = (\mathbf{m}\mathbf{1}^\top + \mathbf{1}\mathbf{m}^\top) / 2$, etc. We select *harmonic mean* by default as it performed better in our experiments. In SIM, the background patch focusing on itself is not in-

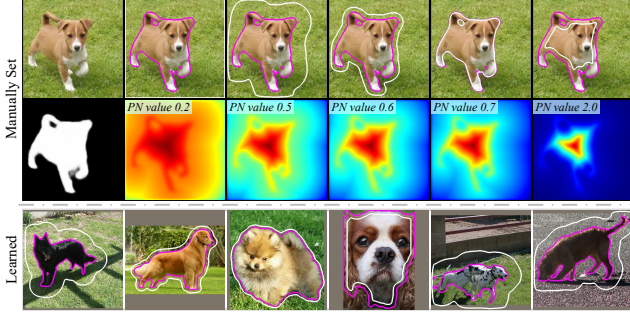


Figure 3. The illustration of power normalization (PN). The top images show the effects when PN values are *manually set* while the bottom images show the morphology *learned* by our ML.

cluded. Thus, a term $\mathbb{I} - \text{Diag}(\mathbf{m})$ is added to form the attention mask $\tilde{\mathbf{M}} \in \mathbb{R}^{n \times n}$ as

$$\tilde{\mathbf{M}} = \bar{\mathbf{M}} + \mathbb{I} - \text{Diag}(\mathbf{m}), \quad (5)$$

where $\text{Diag}(\mathbf{m}) \in \mathbb{R}^{n \times n}$ is the diagonal matrix of \mathbf{m} . A property of $\tilde{\mathbf{M}}$ is the diagonal elements are all *unit*. By treating $\tilde{\mathbf{M}}$ as a bias, we formulate soft M-SA as

$$\mathbf{A} = \gamma(\psi(\mathbf{Q}, \mathbf{K}, \mathbf{M})) = \gamma(\phi(\mathbf{Q}, \mathbf{K}) - (\mathbf{1}\mathbf{1}^\top - \tilde{\mathbf{M}})J), \quad (6)$$

where J is a scalar that controls the degree of masking, and (γ, ϕ) is the softmax SA or RBF SA. In contrast to hard masking in Eq. 4, one can back-propagate through Eq. 6 of soft M-SA. Also, compared to the global attention of vanilla SA (Eq. 2), our M-SA facilitates relation learning in salient areas.

Property of M-SA: If the whole image is salient, *i.e.*, $\mathbf{m} = \mathbf{1} \in \mathbb{R}^n$, then $\bar{\mathbf{M}} = \bar{\mathbf{M}} = \mathbf{1}\mathbf{1}^\top \in \mathbb{R}^{n \times n}$. Thus, $\gamma(\psi(\mathbf{Q}, \mathbf{K}, \mathbf{M})) = \gamma(\phi(\mathbf{Q}, \mathbf{K}))$ which recovers the vanilla SA. If the whole image is non-salient, *i.e.*, $\mathbf{m} = \mathbf{0}$, then $\bar{\mathbf{M}} = \mathbf{0}$, $\tilde{\mathbf{M}} = \mathbb{I}$ then $\gamma(\psi(\mathbf{Q}, \mathbf{K}, \mathbf{M})) = \gamma(\phi(\mathbf{Q}, \mathbf{K}) - (\mathbf{1}\mathbf{1}^\top - \mathbb{I})J)$ which means that all attention entries are masked except for the diagonal (M-SA learns no relations).

3.2.3 Morphology Learner

Although M-SA can directly use the downscaled saliency map \mathbf{M}^\downarrow , it lacks adaptation to the context of object. To endow SalViT with a “dynamic receptive field”, we propose the morphology learner (ML) which modifies \mathbf{M}^\downarrow . As shown in Fig. 2(a), the morphology learner consists of a morphology parameter generator (MPG) and a morphology changing module (MCM). Firstly, we adopt a saliency embedding module (SEM) to encode saliency map and RGB image into saliency embeddings $\mathbf{F}^{\text{sal}} \in \mathbb{R}^{n \times d_e}$ (Fig. 2(b)). Then, the patch features \mathbf{P} and \mathbf{F}^{sal} are concatenated and globally average-pooled as $\mathbf{F} = \text{GAP}([\mathbf{F}^{\text{sal}}, \mathbf{P}]) \in \mathbb{R}^{(d+d_e)}$ and fed to MPG to predict parameter θ as

$$\theta = \mathbf{W}_2 \text{GeLU}(\mathbf{W}_1 \mathbf{F} + \mathbf{b}_1) + \mathbf{b}_2. \quad (7)$$

Finally, θ is injected into MCM to control the morphology of \mathbf{M}^\downarrow via *power normalization* as

$$\tilde{\theta} = \rho_1 \cdot \text{sigmoid}(\theta), \quad \mathbf{M} = (\mathbf{M}^\downarrow)^{\tilde{\theta}}, \quad (8)$$

where $\rho_1 \in \mathbb{R}$ controls the bound of morphology ($0 \leq \tilde{\theta} \leq \rho_1$). To ensure $\tilde{\theta}$ changes properly, we regularize it by $\mathcal{L}_{\text{reg}} = \mathbb{E}[\max((\tilde{\theta} - \rho_2)^2 - \rho_3, 0)]$, where ρ_2 is the desired morphology center and ρ_3 is the interval. We set $\rho_1 = 2$, $\rho_2 = 0.7$, and $\rho_3 = 0.05$. Thus, matrix \mathbf{M} (or \mathbf{m} in vectorized form) is learned to help M-SA focus on foregrounds and the context (Fig. 3).

3.3. Few-shot Keypoint Detection

Based on SalViT, we propose our few-shot keypoint detection (FSKD) pipeline, as shown in Fig. 4. For K support images and N support keypoints per image, FSKD detects the corresponding keypoints in a query image (*N-way-K-shot detection*). Our FSKD model includes SalViT-based feature encoder \mathcal{E} , feature modulator \mathcal{M} , descriptor net \mathcal{D} , and keypoint localization net \mathcal{G} . Features of \mathcal{E} capture relations between salient patches, which helps modulator \mathcal{M} .

Fig. 2(c) shows the architecture of \mathcal{E} , which takes saliency/RGB $\mathbf{I} = [\mathbf{I}^{\text{sal}}; \mathbf{I}^{\text{rgb}}]$ as inputs, and outputs ensemble features $\mathcal{E}(\mathbf{I})$ that encode foreground patch relations.

Inductive Inference: Let the k -th support image with saliency \mathbf{I}_k^s be encoded as $\mathcal{E}(\mathbf{I}_k^s) \in \mathbb{R}^{l \times l \times d}$, and $\mathbf{X}_{k,n}^s$ is the n -th support keypoint in the k -th support image. Firstly, we extract support keypoint representation (SKR) $\Phi_{k,n} \in \mathbb{R}^d$ via Gaussian pooling. Following PrototNet [33], we form the support keypoint prototype (SKP) to represent each type of keypoints by averaging the SKRs across support images, *i.e.*, $\mathbf{c}_n = \frac{1}{K} \sum_{k=1}^K \Phi_{k,n}$. Thus, N SKPs are produced for *N-way-K-shot* detection. Subsequently, the SKPs are used to modulate query feature map $\mathcal{E}(\mathbf{I}^q) \in \mathbb{R}^{l \times l \times d}$ via \mathcal{M} , yielding the attentive feature map $\mathbf{F}_n^{\text{att}} = \mathcal{M}(\mathcal{E}(\mathbf{I}^q), \mathbf{c}_n) \in \mathbb{R}^{l \times l \times d}$ per SKP, where $\mathbf{F}_n^{\text{att}}(\mathbf{p}) = \mathcal{E}(\mathbf{I}^q)(\mathbf{p}) \odot \mathbf{c}_n$ and \odot refers channel-wise multiplication. Thus \mathcal{M} correlates SKPs with similar regions in the query image. Each $\mathbf{F}_n^{\text{att}}$ is then processed into descriptor Ψ_n via \mathcal{D} and fed to a multi-scale grid-based localization net \mathcal{G} to predict keypoint $\mathbf{x} \in \mathbb{R}^2$ and uncertainty $\Sigma \in \mathbb{R}^{2 \times 2}$.

Fig. 4 shows that each scale of localization net $\mathcal{G}^{(S)}$ includes three branches: grid classifier \mathcal{G}_c , offset regressor \mathcal{G}_o , and covariance branch \mathcal{G}_v , which predict grid probability map $\mathbf{P} = \text{softmax}(\mathcal{G}_c(\Psi_n)) \in \mathbb{R}^{S \times S}$, offset vector field $\mathbf{O} = \mathcal{G}_o(\Psi_n) \in \mathbb{R}^{S \times S \times 2}$, and latent covariance field $\mathbf{V} = \mathcal{G}_v(\Psi_n) \in \mathbb{R}^{S \times S \times 2d_v}$, respectively. The grid $\mathbf{g} \in \{0, \dots, S-1\} \times \{0, \dots, S-1\}$. Accordingly, we extract offset $\mathbf{o} = \mathcal{O}(\mathbf{g}) \in [-1, 1]^2$ and latent covariance $\mathbf{Q} = \mathbf{V}(\mathbf{g}) \in \mathbb{R}^{2d_v}$ using \mathbf{g} . In this paper, we regress precision matrix $\Omega = \tilde{\mathbf{Q}}(\mathbf{Q})^\top / d_v$ instead of covariance Σ to avoid inverting covariance in the loss function, where

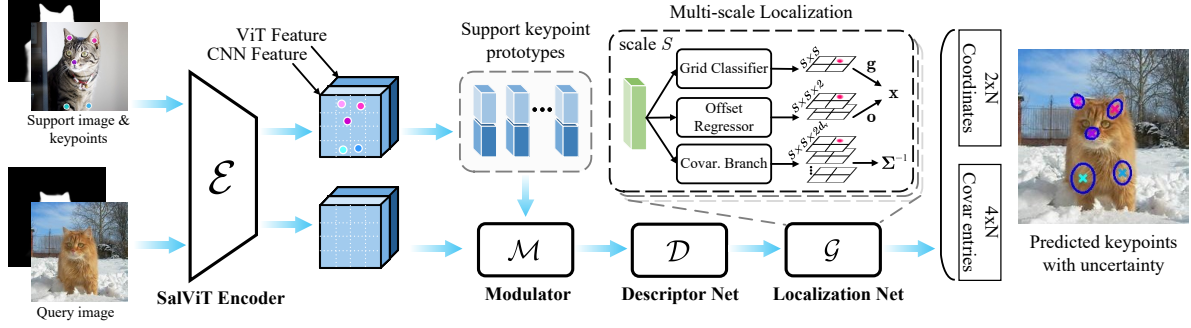


Figure 4. Overview of the proposed few-shot keypoint detection pipeline with SalViT.

$\tilde{\mathbf{Q}} \in \mathbb{R}^{2 \times d_v}$ is reshaped from \mathbf{Q} . We form the grid classification loss \mathcal{L}_{cls} and offset regression loss \mathcal{L}_{os} as

$$\mathcal{L}_{\text{cls}} = -\mathbb{E} \log \mathbf{P}(\hat{\mathbf{g}}), \mathcal{L}_{\text{os}} = \frac{1}{2} \mathbb{E}[(\mathbf{x} - \hat{\mathbf{x}})^\top \boldsymbol{\Omega}(\mathbf{x} - \hat{\mathbf{x}}) - \log \det(\boldsymbol{\Omega})], \quad (9)$$

where $\hat{\mathbf{g}}$ and $\hat{\mathbf{x}}$ are groundtruth grid and offset. If \mathcal{G} has N_S scales $\{S_i\}_{i=1}^{N_S}$, the multi-scale localization loss is $\mathcal{L}_{\text{ms}} = \sum_{i=1}^{N_S} (\mathcal{L}_{\text{cls}}^{(S_i)} + \mathcal{L}_{\text{os}}^{(S_i)}) / N_S$. Moreover, the multi-scale prediction is obtained as

$$\mathbf{x} = \frac{1}{N_S} \sum_{i=1}^{N_S} \frac{l_0}{S_i} \left(\mathbf{g}^{(S_i)} + 0.5 + 0.5 \mathbf{o}^{(S_i)} \right), \quad (10)$$

$$\boldsymbol{\Sigma} = \frac{1}{4N_S} \sum_{i=1}^{N_S} \left(\frac{l_0}{S_i} \right)^2 \boldsymbol{\Sigma}^{(S_i)}$$

where l_0 is the edge length of square-padded query image, $\boldsymbol{\Sigma}^{(S_i)}$ is the inverse of $\boldsymbol{\Omega}^{(S_i)}$ at scale S_i .

Masking and Alignment (MAA): Even though ViT is known to be robust to occlusions [30], it fails under severe occlusions over keypoints (see Table 8). Inspired by [50], we propose to randomly mask input $\mathbf{I} = [\mathbf{I}^{\text{sal}}, \mathbf{I}^{\text{rgb}}]$ to form an occluded view \mathbf{I}^{occ} . We define localization loss on occluded inputs as $\mathcal{L}_{\text{ms}}^{\text{occ}}$. Then we form an alignment loss \mathcal{L}_{aln} by the KL divergence $\text{KL}[\mathbf{P} | | \mathbf{P}^{\text{occ}}]$ or $\|\mathcal{E}(\mathbf{I}) - \mathcal{E}(\mathbf{I}^{\text{occ}})\|$ with the l_1 or l_2 loss. \mathbf{P} (or \mathbf{P}^{occ}) and $\mathcal{E}(\mathbf{I})$ (or $\mathcal{E}(\mathbf{I}^{\text{occ}})$) refer to grid probability maps and features of non-occluded (or occluded) inputs. In experiments we investigate the best strategy to perform MAA. Including the regularization loss \mathcal{L}_{reg} obtained from \mathcal{E} , the total loss becomes

$$\mathcal{L} = \lambda_1 \mathcal{L}_{\text{ms}}^{\text{occ}} + \lambda_2 \mathcal{L}_{\text{reg}} + \lambda_3 \mathcal{L}_{\text{aln}}, \quad (11)$$

where we set $\lambda_1 = \lambda_2 = 0.5$, $\lambda_3 = 0.1$ by default.

Transductive Inference: FSKD has to represent prototype \mathbf{c}_n for each kind of support keypoints well, and measure its similarity w.r.t. the query feature. As support samples are limited, SKP \mathbf{c}_n cannot represent the true keypoint well. Thus, we extend FSKD to the transductive setting by leveraging the unlabeled query samples.

Let SKRs be $\mathcal{S} \equiv \{\Phi_{k,n}\}_{k,n=1}^{K \times N}$ and the SKRs of n -th keypoint type be $\mathcal{S}^{(n)} \equiv \{\Phi_{k,n}\}_{k=1}^K$. Let the initial SKPs

$\mathcal{C} \equiv \{\mathbf{c}_n\}_{n=1}^N$ be formed based on \mathcal{S} . For each query image and each prototype, we retrieve top- W query keypoints. For Z query images, we get $\{\mathbf{x}_{z,n,w}\}_{z,n,w=1}^{Z \times N \times W}$, by selecting the top- W grids from the grid probability map. Then we define the label confidence criterion by using the corresponding keypoint probability scores $\{p_{z,n,w}\}_{z,n,w=1}^{Z \times N \times W}$, rank the scores per keypoint type in descending order, and select top- η query keypoints per type to generate the candidate set $\mathcal{Q}^{(n)} \equiv \{\tilde{\Phi} : \tilde{\Phi} = \mathcal{E}(\mathbf{I}_z^q)(\mathbf{x}_{z,n,w}), B_{z,w}^{(n)} = 1, \forall z, w\}$, where $\mathcal{E}(\mathbf{I}_z^q)(\mathbf{x}_{z,n,w})$ is the keypoint representation extracted at $\mathbf{x}_{z,n,w}$ from the query image \mathbf{I}_z^q , $\mathbf{B}^{(n)} \in \{0, 1\}^{Z \times W}$ denotes the selection indicator for the n -th type of predicted query keypoints, which is $\mathbf{B}^{(n)} = \arg \max_{\|\mathbf{B}^{(n)}\|_0 = \eta} \sum_{z,w=1}^{Z \times W} p_{z,n,w} B_{z,w}^{(n)}$. Based on the candidate set $\mathcal{Q}^{(n)}$, we refine SKPs by the *soft assignment* as

$$\mathbf{c}_n^* = \frac{1}{\kappa |\mathcal{S}^{(n)}| + (1 - \kappa) \sum_{\tilde{\Phi} \in \mathcal{Q}^{(n)}} p(\tilde{\Phi}, \mathbf{c}_n)} \left(\kappa \sum_{\Phi \in \mathcal{S}^{(n)}} \Phi + (1 - \kappa) \sum_{\tilde{\Phi} \in \mathcal{Q}^{(n)}} p(\tilde{\Phi}, \mathbf{c}_n) \tilde{\Phi} \right), \quad (12)$$

where $0 \leq \kappa \leq 1$ controls the amount of added pseudo-label information, and $p(\tilde{\Phi}, \mathbf{c}_n) = \exp(-\|\tilde{\Phi} - \mathbf{c}_n\| / 2\sigma^2) / \sum_{i=1}^N \exp(-\|\tilde{\Phi} - \mathbf{c}_i\| / 2\sigma^2)$ is the assignment probability given \mathbf{c}_n . The updated SKP \mathbf{c}_n^* is more representative and utilized to re-estimate query keypoints.

4. Experiments

4.1. Settings

Datasets: We conduct FSKD experiments on *five* datasets. *Animal pose* dataset [5] has five mammal species *cat*, *dog*, *cow*, *horse*, and *sheep*, with 6000+ instances with keypoint annotations. *CUB* [39] and *NABird* [36] have 200 and 555 categories, respectively. *AwA* [1] has 35 animal species with 10064 images. *DeepFashion2* [17] is a large-scale clothing dataset with 13 categories and 8~39 landmarks.

Metric: The percentage of correct keypoints (PCK) [45] is used. A predicted keypoint is correct if its distance to GT $d \leq \tau \cdot \max(w_{\text{bbx}}, h_{\text{bbx}})$, where w_{bbx} and h_{bbx} are the edges of object bounding box, and $\tau = 0.1$.

Table 2. Results on few-shot keypoint detection for unseen species across four datasets. The harmonic mean of PCK scores on novel and base keypoint detection is reported. Symbol **+T** refers to applying transductive inference during testing. **IT** is keypoint inference time per query image. The best and second best scores are marked in **red** and **blue**.

Shots	Model	Params	IT	Animal Pose Dataset						CUB	NABird	AwA
				Cat	Dog	Cow	Horse	Sheep	Avg			
1-shot	ProbIntr [31]	29.5M	3.8 ms	35.21	30.01	25.79	24.87	23.33	27.84	70.66	57.63	40.65
	ProtoNet [33]	19.0M	3.4 ms	27.53	23.01	20.37	18.03	20.55	21.90	62.64	48.84	38.98
	RelationNet [34]	21.1M	3.6 ms	30.89	25.01	22.29	20.52	22.91	24.32	66.08	47.53	30.64
	WG (w/o Att.) [18]	19.0M	3.9 ms	30.70	24.87	23.58	23.23	22.63	25.00	63.64	47.18	38.85
	WG [18]	23.2M	4.1 ms	31.02	27.04	24.25	23.80	23.40	25.90	65.65	48.15	39.45
	FSKD-R [29]	65.2M	3.9 ms	50.99	45.29	42.07	43.13	36.61	43.62	82.62	66.89	57.76
	FSKD-D [29]	65.2M	3.9 ms	54.30	49.56	46.06	46.01	39.94	47.17	82.51	68.17	65.56
	SalViT (DINO)	50.9M	4.9 ms	55.75	50.29	46.90	47.23	41.66	48.37	84.50	69.45	69.75
	SalViT (default)	56.9M	4.5 ms	57.00	50.94	48.13	47.87	42.36	49.26	84.62	69.58	68.18
SalViT (default)+T	56.9M	6.6 ms	59.94	54.82	52.06	50.01	45.61	52.49	88.36	72.47	70.79	
5-shot	ProbIntr [31]	29.5M	4.9 ms	43.83	40.06	33.41	36.24	29.47	36.60	78.78	68.76	53.23
	ProtoNet [33]	19.0M	4.6 ms	35.23	31.11	30.25	29.77	28.42	30.96	71.81	64.56	46.43
	RelationNet [34]	21.1M	4.6 ms	33.24	28.75	29.69	26.38	29.06	29.42	70.43	55.58	40.06
	WG (w/o Att.) [18]	19.0M	5.0 ms	30.41	28.13	29.64	32.15	27.64	29.59	72.52	60.70	45.90
	WG [18]	23.2M	5.1 ms	40.11	36.14	34.67	35.61	31.47	35.60	71.95	60.98	50.87
	FSKD-R [29]	65.2M	4.9 ms	59.43	52.59	53.13	55.04	46.43	53.33	86.99	75.66	71.59
	FSKD-D [29]	65.2M	4.9 ms	61.33	55.62	56.19	55.11	49.25	55.50	86.17	75.50	74.84
	SalViT (DINO)	50.9M	6.4 ms	62.03	58.65	57.41	56.69	50.47	57.05	88.18	76.65	79.41
	SalViT (default)	56.9M	5.5 ms	62.24	57.33	57.93	57.33	50.50	57.07	87.76	77.08	76.77
SalViT (default)+T	56.9M	7.6 ms	64.49	59.29	60.39	59.91	53.01	59.42	89.81	78.85	81.03	

Baseline Methods: Firstly, we adapt *ProbIntr* [31] trained jointly by self-supervised keypoints and labeled query keypoints for comparison. Then, popular few-shot learning approaches *ProtoNet* [33], *RelationNet* [34], and *WG* (with or w/o attention) [18] are adapted to FSKD. Moreover, *FSKD-R* [29] and *FSKD-D* [29] are compared, which respectively uses random or default auxiliary keypoints during training. Following [29], we also use default auxiliary keypoints to boost keypoint generalization. We present two models for comparison, which are *SalViT (default)* and *SalViT (DINO)*. All is same except the former exploits CNN as backbone and MNL saliency [48], while the latter uses pre-trained DINO [7] and its class token attentiveness as saliency.

Implementation Details: The input size to all models is 384×384 . For *SalViT (default)* model, the backbone uses ResNet50 [20], which has 23M params and is commonly used in detection with transformer, e.g., DETR [6]. For *SalViT (DINO)*, we choose DINO ViT-S/16 (21M params) pre-trained on ImageNet 1K [11] as backbone. The first 10 layers of DINO ViT are frozen and the class token attentiveness is taken from frozen layers due to better generalization that produces better ‘‘saliency’’ (see Sec. A.1 in Suppl. for vis.) By default, we use one *SalViT* with RBF-based M-SA, set the temperature $\beta = 1$ and the degree of masking $J = 1$. To keep *SalViT* light-weight, token dim. is set to 384 as in ViT-S. All models are trained with 40k episodes. The scores are averaged over 1000 episodes in testing. In transductive inference, the number of test query images is 60.

Table 3. 1-shot/5-shot novel keypoint detection on DeepFashion2. The metric of NE (normalized error $d' = d / \max(w_{\text{img}}, h_{\text{img}})$) and PCK with 95% confidence intervals are used. The results marked with * are from [16]. ‘-’: no reported results.

Method	1-shot		5-shot	
	PCK (\uparrow)	NE (\downarrow)	PCK (\uparrow)	NE (\downarrow)
MAML* [15]	-	0.215 \pm 0.023	-	0.126 \pm 0.017
ProtoNet* [33]	-	0.179 \pm 0.042	-	0.135 \pm 0.039
WG* [18]	-	0.185 \pm 0.051	-	0.160 \pm 0.047
FSKD [29]	33.04 \pm 1.80	0.149 \pm 0.005	44.92 \pm 1.72	0.111 \pm 0.004
MetaCloth* [16]	-	0.145 \pm 0.021	-	0.096 \pm 0.015
SalViT (DINO)	35.59 \pm 1.38	0.134 \pm 0.004	48.00 \pm 1.31	0.089 \pm 0.002
SalViT (default)	36.15 \pm 1.46	0.130 \pm 0.004	50.52 \pm 1.32	0.087 \pm 0.003

4.2. Comparisons on Few-shot Keypoint Detection

All compared FSKD models are trained on seen species with base keypoints, and tested on unseen species with novel (or base) keypoints. The split settings of seen and unseen species, novel and base keypoints across five datasets are same to work [29]. For Animal pose dataset, one animal species is alternately chosen as unseen species for testing while the remaining four as seen species for training, which yields five subproblems. For AwA, 25 species are for training and 10 for testing. For DeepFashion2, 6 upper-body clothing categories are set as seen categories and 7 lower-body clothing categories are set as unseen ones [16, 29].

Table 2 shows our model variants *SalViT (default)* and *SalViT (DINO)* consistently obtain higher harmonic scores of novel and base keypoint detection across all tasks, and enjoy significant improvements. For 1-shot setting, our *SalViT (default)* outperforms previous state-of-the-art

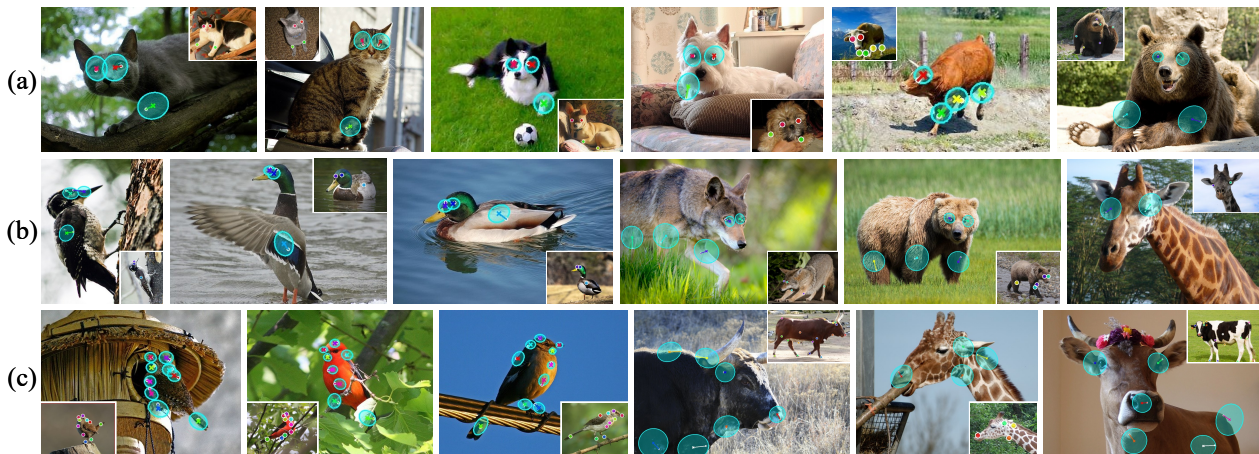


Figure 5. Visualization of few-shot keypoint detection for unseen species. Rows (a) and (b) show the results on detecting novel keypoints while (c) shows detected base keypoints. The support image & keypoints are in the corner of each query image. Dots, tilted crosses, and ellipses refer to GT, predicted keypoints and uncertainty, respectively. The line that links prediction and GT reflects the localization error.

Table 4. Ablation study of SalViT in 1-shot novel keypoint detection. The result on Animal is the average of five subproblems.

Models	Animal	CUB	NABird	AwA
<i>DINO w. ViT</i>	44.03	76.96	56.11	66.25
<i>DINO w. SalViT</i>	45.71	80.08	57.19	68.71
<i>CNN-only</i>	44.25	76.54	54.71	61.75
<i>ViT-only</i>	43.19	76.71	54.44	62.53
<i>CNN+ViT</i>	44.34	76.62	54.57	63.22
<i>SalViT</i>	46.61	79.52	57.36	67.74
<i>SalViT (w/o ML)</i>	44.79	77.70	56.66	64.19
<i>SalViT (w/o PE)</i>	45.02	77.03	55.41	65.23

model FSKD-D [29] by 2.09% in Animal Avg, 2.11% in CUB, 1.41% in NABird, and 2.62% in AwA. Our SalViT (DINO) performs very well on AwA, and achieves 4.19% improvement in 1-shot setting and 4.57% in 5-shot setting. Moreover, both model variants have fewer parameters than FSKD-D at the expense of slightly longer inference time. The higher scores explain the effectiveness of SalViT in detecting few-shot keypoints by learning foreground patch relations. Even though the saliency prior of DINO is not as good as MNL prior (see Table 1), it achieves very competitive scores. We conjecture it may be due to the function of morphology learner (ML) inside SalViT, which refines lower quality saliency priors.

By applying transductive inference, the performance is further improved. Compared to our SalViT (default), the transductive version obtains further gains of 3.23% in Animal Avg, and 3.74% in CUB in 1-shot setting. The stronger performance indicates that the unlabeled data enhances keypoint representations and benefits FSKD. Table 3 shows our SalViT achieves higher PCK scores yet lower NE error in DeepFashion2 dataset. Fig. 5 shows the qualitative results of our approach, which manifests its effectiveness to localize keypoints and estimate keypoint uncertainty.

4.3. Ablation Studies

The ablations are performed using our SalViT (default) model on novel keypoint detection for unseen species.

Salient Patch Relations: When using DINO as backbone, Table 4 (top part) shows SalViT (DINO) greatly beats DINO with vanilla ViT. In CUB, SalViT (DINO) enjoys 3.12% gain. When using CNN as backbone, compared to CNN-only (relies on neighborhood information), or ViT-only (relies on global patch relations), Table 4 (middle part) shows our SalViT consistently performs best, e.g., 4.52% improvements in AwA than CNN+ViT, validating the effectiveness of capturing salient patch relations by our soft M-SA.

Morphology Learner (ML): When turning off ML in SalViT, we observe losses across four datasets (lower part, Table 4). The similar losses appear if position encoding (PE) is not used. These observations reflect the importance of adapting receptive field in M-SA and incorporating spatial information for keypoint inference. Moreover, we manually set or automatically learn PN value in ML. Table 5 shows that morphology learning improves scores.

Transductive Inference: As transductive inference relies on the quality of pseudo labels, we firstly capture the upper bound of performance using the GT keypoints of queries to select high-quality pseudo labels. Then, we compare the employed soft assignment (SM) against the simple average-based SKP refinement. Table 6 shows our approach yields higher scores closer to the upper bound.

Saliency Detectors & Saliency Failures: Fig. 6(a) shows SalViT with unsupervised MNL or DINO yields performance close to SCRN in 1-shot setting (and better in 5-shot). Although better saliency prior improves performance, our ML leverages saliency maps efficiently, mitigating the influence of low-quality maps. Moreover, we test the trained model under simulated saliency failures. Fig. 6(b) shows performance of SalViT drops a little under

Table 5. Influence of power normalization (PN) value on SalViT in FSKD. The *auto* means using learnable PN, namely turning on the morphology learner (ML) in SalViT.

Datasets	0.2	0.5	0.7	0.8	1.0	2.0	auto
Animal	43.56	44.14	45.32	44.63	44.81	44.16	46.61
AwA	61.53	61.57	63.58	62.94	62.23	61.29	67.74

Table 6. Ablation of prototype refinement approaches in transductive FSKD. Harmonic scores of 1-shot setting are reported.

Method	Animal	AwA
<i>Inductive</i> (baseline)	49.26	68.18
<i>Trans.</i> +Avg	50.27 (+1.01)	69.17 (+0.99)
<i>Trans.</i> +SM (ours)	52.49 (+3.23)	70.79 (+2.61)
<i>Trans.</i> +GT	54.23 (+4.97)	73.09 (+4.91)

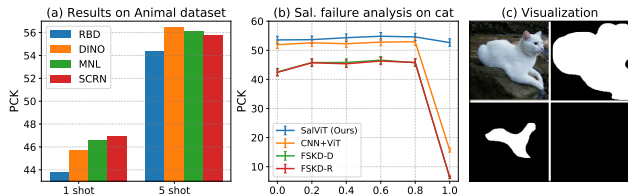


Figure 6. Results on SalViT with (a) different saliency detectors & (b)-(c) simulated saliency failures by varying saliency thresholds.

Table 7. Ablations of occlusion handling with various masking strategies. Tick \checkmark indicates applying foreground patch masking over RGB image, saliency map, or CNN patch features; no tick means no masking. Each row indicates a masking strategy for FSKD model training. The model is tested under various occlusion probabilities p of query keypoints. The higher the p is, the more severe the occlusions are. Average PCKs of novel keypoint detection on *five* subproblems in Animal pose dataset are given.

RGB	Sal.	Feat.	0%	30%	50%	100%
			45.60	38.49	34.05	22.82
\checkmark			45.60	40.49	37.94	30.27
\checkmark	\checkmark		46.28	40.68	37.70	29.77
\checkmark	\checkmark	\checkmark	46.04	40.75	37.42	29.13
	\checkmark	\checkmark	46.18	38.84	34.63	23.74

large saliency failures. If foreground (FG) is available, FG relations between tokens are captured by our M-SA. When FG is removed, then each token uses self-relation (identity matrix in Eq. 5). Such a property of M-SA ensures signal flows through attention even for bad saliency failures. We also equip other models with saliency by re-weighting patch features for refinement but that helps little under failures.

4.4. FSKD Under Occlusions

Below we investigate if our masked self-attention is robust to keypoint occlusions, and consider various strategies to improve the ability of our model to handle occlusions.

Firstly, we test the normally-trained FSKD model under different occlusion probability to query keypoints. Each testing occlusion block is centered at query keypoint and has random size with an area ratio to object bounding box between 0.01 and 0.04 and aspect ratio between 0.7 and 1.4.

Table 8. Ablations of various masking and alignment (MAA) strategies. The results are the average of five subproblems in Animal pose dataset. Non-Occl means adding the prediction loss from non-occluded images. Y: applied; N: not applied.

Mask	Alignment	0%	50%	100%
N	N	45.60	34.05	22.82
Y	N	46.28	37.70	29.77
Y	SimMIM [44]	46.10	38.15	30.61
Y	Non-Occl Loss	45.65	37.15	28.22
Y	Feat. Align (MMD)	45.44	36.68	28.52
Y	Feat. Align (ℓ_2)	46.29	38.21	29.68
Y	Feat. Align (ℓ_1)	46.80	38.22	30.13
Y	Prob. Align	46.74	38.40	32.04

Secondly, we explore masking different cues during training: RGB image, saliency map, and CNN patch features. Between 2 and 12 foreground patches in RGB image are randomly masked with gray box, saliency and CNN features are masked with zero values. The FSKD model is trained by various masking strategies and tested under occluded query keypoints. Table 7 shows that with no masking applied, the normally-trained FSKD model is unable to handle occlusions well. Masking RGB image, RGB + Saliency, RGB + Saliency + CNN patch features show higher yet similar results towards occlusions of *background crop* even though trained with occlusions of *gray box*. Moreover, on top of masking inputs, we investigate different alignment approaches: 1) alignment in *image space* using SimMIM [44]; 2) alignment in *predictions* by adding the loss over non-occluded image (*i.e.* Non-Occl); 3) alignment in *feature space* with various distance metrics including ℓ_1 , ℓ_2 , and MMD [2]; and 4) alignment in *probability maps*. Table 8 shows that using the probability alignment is the most effective, boosting scores by up to 2% compared to masking-only, and by 10% compared to the normally trained model with no MAA strategy under 100% occlusions.

5. Conclusions

We have introduced a saliency-guided vision transformer, SalViT, for few-shot keypoint detection. The key insight is to learn the foreground patch relations via SalViT and use such relations for similarity learning in FSKD. The SalViT includes a uniquely designed masked self-attention (M-SA) and a morphology learner (ML), which together constrain self-attention within salient regions while allowing adaptation. Moreover, we have presented a transductive FSKD variant in addition to the standard inductive inference. The FSKD benchmarks across five datasets highlight that our FSKD with SalViT achieves competitive results. The extensive experiments show the effectiveness of M-SA and ML. The occlusion setting reveals that our SalViT-based model with proper masking and alignment handles occlusions of keypoints well. Finally, saliency detectors and backbone can be readily replaced by DINO.

References

- [1] Prianka Banik, Lin Li, and Xishuang Dong. A novel dataset for keypoint detection of quadruped animals from images. *arXiv preprint arXiv:2108.13958*, 2021. 3, 5
- [2] Karsten M Borgwardt, Arthur Gretton, Malte J Rasch, Hans-Peter Kriegel, Bernhard Schölkopf, and Alex J Smola. Integrating structured biological data by kernel maximum mean discrepancy. *Bioinformatics*, 22(14):e49–e57, 2006. 8, 15
- [3] Tom Brown, Benjamin Mann, Nick Ryder, Melanie Subbiah, Jared D Kaplan, Prafulla Dhariwal, Arvind Neelakantan, Pranav Shyam, Girish Sastry, Amanda Askell, et al. Language models are few-shot learners. *Advances in neural information processing systems*, 33:1877–1901, 2020. 2
- [4] Yuanhao Cai, Jing Lin, Xiaowan Hu, Haoqian Wang, Xin Yuan, Yulun Zhang, Radu Timofte, and Luc Van Gool. Mask-guided spectral-wise transformer for efficient hyperspectral image reconstruction. In *Proceedings of the IEEE/CVF Conference on Computer Vision and Pattern Recognition*, pages 17502–17511, 2022. 2
- [5] Jinkun Cao, Hongyang Tang, Hao-Shu Fang, Xiaoyong Shen, Cewu Lu, and Yu-Wing Tai. Cross-domain adaptation for animal pose estimation. In *Proceedings of the IEEE/CVF International Conference on Computer Vision*, pages 9498–9507, 2019. 3, 5
- [6] Nicolas Carion, Francisco Massa, Gabriel Synnaeve, Nicolas Usunier, Alexander Kirillov, and Sergey Zagoruyko. End-to-end object detection with transformers. In *Computer Vision—ECCV 2020: 16th European Conference, Glasgow, UK, August 23–28, 2020, Proceedings, Part I 16*, pages 213–229. Springer, 2020. 6
- [7] Mathilde Caron, Hugo Touvron, Ishan Misra, Hervé Jégou, Julien Mairal, Piotr Bojanowski, and Armand Joulin. Emerging properties in self-supervised vision transformers. In *Proceedings of the IEEE/CVF International Conference on Computer Vision*, pages 9650–9660, 2021. 2, 3, 6, 12, 13
- [8] Chun-Fu Richard Chen, Quanfu Fan, and Rameswar Panda. Crossvit: Cross-attention multi-scale vision transformer for image classification. In *Proceedings of the IEEE/CVF international conference on computer vision*, pages 357–366, 2021. 2
- [9] Bowen Cheng, Ishan Misra, Alexander G Schwing, Alexander Kirillov, and Rohit Girdhar. Masked-attention mask transformer for universal image segmentation. In *Proceedings of the IEEE/CVF Conference on Computer Vision and Pattern Recognition*, pages 1290–1299, 2022. 2
- [10] Xiangxiang Chu, Zhi Tian, Yuqing Wang, Bo Zhang, Haibing Ren, Xiaolin Wei, Huaxia Xia, and Chunhua Shen. Twins: Revisiting the design of spatial attention in vision transformers. *Advances in Neural Information Processing Systems*, 34:9355–9366, 2021. 2
- [11] Jia Deng, Wei Dong, Richard Socher, Li-Jia Li, Kai Li, and Li Fei-Fei. Imagenet: A large-scale hierarchical image database. In *2009 IEEE conference on computer vision and pattern recognition*, pages 248–255. Ieee, 2009. 6
- [12] Jacob Devlin, Ming-Wei Chang, Kenton Lee, and Kristina Toutanova. Bert: Pre-training of deep bidirectional transformers for language understanding. *arXiv preprint arXiv:1810.04805*, 2018. 2
- [13] Alexey Dosovitskiy, Lucas Beyer, Alexander Kolesnikov, Dirk Weissenborn, Xiaohua Zhai, Thomas Unterthiner, Mostafa Dehghani, Matthias Minderer, Georg Heigold, Sylvain Gelly, et al. An image is worth 16x16 words: Transformers for image recognition at scale. In *International Conference on Learning Representations*, 2021. 2
- [14] Qi Fan, Wei Zhuo, Chi-Keung Tang, and Yu-Wing Tai. Few-shot object detection with attention-rpn and multi-relation detector. In *Proceedings of the IEEE/CVF Conference on Computer Vision and Pattern Recognition*, pages 4013–4022, 2020. 1
- [15] Chelsea Finn, Pieter Abbeel, and Sergey Levine. Model-agnostic meta-learning for fast adaptation of deep networks. In *International Conference on Machine Learning*, pages 1126–1135. PMLR, 2017. 2, 6
- [16] Yuying Ge, Ruimao Zhang, and Ping Luo. Metacloth: Learning unseen tasks of dense fashion landmark detection from a few samples. *IEEE Transactions on Image Processing*, 31:1120–1133, 2021. 1, 6, 13
- [17] Yuying Ge, Ruimao Zhang, Xiaogang Wang, Xiaoou Tang, and Ping Luo. Deepfashion2: A versatile benchmark for detection, pose estimation, segmentation and re-identification of clothing images. In *Proceedings of the IEEE/CVF Conference on Computer Vision and Pattern Recognition*, pages 5337–5345, 2019. 5
- [18] Spyros Gidaris and Nikos Komodakis. Dynamic few-shot visual learning without forgetting. In *Proceedings of the IEEE Conference on Computer Vision and Pattern Recognition*, pages 4367–4375, 2018. 1, 6, 13
- [19] Kaiming He, Xinlei Chen, Saining Xie, Yanghao Li, Piotr Dollár, and Ross Girshick. Masked autoencoders are scalable vision learners. In *Proceedings of the IEEE/CVF Conference on Computer Vision and Pattern Recognition*, pages 16000–16009, 2022. 2
- [20] Kaiming He, Xiangyu Zhang, Shaoqing Ren, and Jian Sun. Deep residual learning for image recognition. In *Proceedings of the IEEE conference on computer vision and pattern recognition*, pages 770–778, 2016. 6
- [21] Ruibing Hou, Hong Chang, Bingpeng Ma, Shiguang Shan, and Xilin Chen. Cross attention network for few-shot classification. *Advances in Neural Information Processing Systems*, 32, 2019. 2
- [22] Bingyi Kang, Zhuang Liu, Xin Wang, Fisher Yu, Jiashi Feng, and Trevor Darrell. Few-shot object detection via feature reweighting. In *Proceedings of the IEEE/CVF International Conference on Computer Vision*, pages 8420–8429, 2019. 1
- [23] Gregory Koch, Richard Zemel, Ruslan Salakhutdinov, et al. Siamese neural networks for one-shot image recognition. In *ICML deep learning workshop*, volume 2. Lille, 2015. 1, 2
- [24] Gen Li, Varun Jampani, Laura Sevilla-Lara, Deqing Sun, Jonghyun Kim, and Joongkyu Kim. Adaptive prototype learning and allocation for few-shot segmentation. In *Proceedings of the IEEE/CVF Conference on Computer Vision and Pattern Recognition*, pages 8334–8343, 2021. 1

- [25] Wenbo Li, Zhe Lin, Kun Zhou, Lu Qi, Yi Wang, and Jia Jia. Mat: Mask-aware transformer for large hole image inpainting. In *Proceedings of the IEEE/CVF Conference on Computer Vision and Pattern Recognition*, pages 10758–10768, 2022. [2](#)
- [26] Xiang Li, Tianhan Wei, Yau Pun Chen, Yu-Wing Tai, and Chi-Keung Tang. Fss-1000: A 1000-class dataset for few-shot segmentation. In *Proceedings of the IEEE/CVF Conference on Computer Vision and Pattern Recognition*, pages 2869–2878, 2020. [1](#), [13](#)
- [27] Y Liang. Evit: Expediting vision transformers via token reorganizations. In *International Conference on Learning Representations.*, 2021. [3](#)
- [28] Ze Liu, Yutong Lin, Yue Cao, Han Hu, Yixuan Wei, Zheng Zhang, Stephen Lin, and Baining Guo. Swin transformer: Hierarchical vision transformer using shifted windows. In *Proceedings of the IEEE/CVF International Conference on Computer Vision*, pages 10012–10022, 2021. [2](#)
- [29] Changsheng Lu and Piotr Koniusz. Few-shot keypoint detection with uncertainty learning for unseen species. In *Proceedings of the IEEE/CVF Conference on Computer Vision and Pattern Recognition (CVPR)*, pages 19416–19426, June 2022. [1](#), [2](#), [6](#), [7](#)
- [30] Muhammad Muzammal Naseer, Kanchana Ranasinghe, Salman H Khan, Munawar Hayat, Fahad Shahbaz Khan, and Ming-Hsuan Yang. Intriguing properties of vision transformers. *Advances in Neural Information Processing Systems*, 34:23296–23308, 2021. [2](#), [5](#)
- [31] David Novotny, Samuel Albanie, Diane Larlus, and Andrea Vedaldi. Self-supervised learning of geometrically stable features through probabilistic introspection. In *Proceedings of the IEEE Conference on Computer Vision and Pattern Recognition*, pages 3637–3645, 2018. [6](#)
- [32] Niki Parmar, Ashish Vaswani, Jakob Uszkoreit, Lukasz Kaiser, Noam Shazeer, Alexander Ku, and Dustin Tran. Image transformer. In *International conference on machine learning*, pages 4055–4064. PMLR, 2018. [2](#)
- [33] Jake Snell, Kevin Swersky, and Richard S Zemel. Prototypical networks for few-shot learning. *arXiv preprint arXiv:1703.05175*, 2017. [1](#), [2](#), [4](#), [6](#), [12](#)
- [34] Flood Sung, Yongxin Yang, Li Zhang, Tao Xiang, Philip HS Torr, and Timothy M Hospedales. Learning to compare: Relation network for few-shot learning. In *Proceedings of the IEEE conference on computer vision and pattern recognition*, pages 1199–1208, 2018. [1](#), [2](#), [6](#), [13](#)
- [35] Hugo Touvron, Matthieu Cord, Matthijs Douze, Francisco Massa, Alexandre Sablayrolles, and Hervé Jégou. Training data-efficient image transformers & distillation through attention. In *International Conference on Machine Learning*, pages 10347–10357. PMLR, 2021. [2](#)
- [36] Grant Van Horn, Steve Branson, Ryan Farrell, Scott Haber, Jessie Barry, Panos Ipeirotis, Pietro Perona, and Serge Belongie. Building a bird recognition app and large scale dataset with citizen scientists: The fine print in fine-grained dataset collection. In *Proceedings of the IEEE Conference on Computer Vision and Pattern Recognition*, pages 595–604, 2015. [5](#)
- [37] Ashish Vaswani, Noam Shazeer, Niki Parmar, Jakob Uszkoreit, Llion Jones, Aidan N Gomez, Łukasz Kaiser, and Illia Polosukhin. Attention is all you need. *Advances in neural information processing systems*, 30, 2017. [2](#)
- [38] Oriol Vinyals, Charles Blundell, Timothy Lillicrap, Daan Wierstra, et al. Matching networks for one shot learning. *Advances in neural information processing systems*, 29:3630–3638, 2016. [1](#), [2](#)
- [39] C. Wah, S. Branson, P. Welinder, P. Perona, and S. Belongie. The Caltech-UCSD Birds-200-2011 Dataset. Technical Report CNS-TR-2011-001, California Institute of Technology, 2011. [5](#)
- [40] Xin Wang, Thomas Huang, Joseph Gonzalez, Trevor Darrell, and Fisher Yu. Frustratingly simple few-shot object detection. In *International Conference on Machine Learning*, pages 9919–9928. PMLR, 2020. [1](#)
- [41] Yaqing Wang, Quanming Yao, James T Kwok, and Lionel M Ni. Generalizing from a few examples: A survey on few-shot learning. *ACM Computing Surveys (CSUR)*, 53(3):1–34, 2020. [1](#)
- [42] Zhe Wu, Li Su, and Qingming Huang. Stacked cross refinement network for edge-aware salient object detection. In *Proceedings of the IEEE/CVF International Conference on Computer Vision*, pages 7264–7273, 2019. [3](#), [12](#), [13](#)
- [43] Zhuofan Xia, Xuran Pan, Shiji Song, Li Erran Li, and Gao Huang. Vision transformer with deformable attention. In *Proceedings of the IEEE/CVF Conference on Computer Vision and Pattern Recognition*, pages 4794–4803, 2022. [2](#)
- [44] Zhenda Xie, Zheng Zhang, Yue Cao, Yutong Lin, Jianmin Bao, Zhuliang Yao, Qi Dai, and Han Hu. Simmim: A simple framework for masked image modeling. In *Proceedings of the IEEE/CVF Conference on Computer Vision and Pattern Recognition*, pages 9653–9663, 2022. [2](#), [8](#), [15](#)
- [45] Yi Yang and Deva Ramanan. Articulated human detection with flexible mixtures of parts. *IEEE transactions on pattern analysis and machine intelligence*, 35(12):2878–2890, 2012. [5](#)
- [46] Hongguang Zhang, Jing Zhang, and Piotr Koniusz. Few-shot learning via saliency-guided hallucination of samples. In *Proceedings of the IEEE/CVF Conference on Computer Vision and Pattern Recognition*, pages 2770–2779, 2019. [2](#), [3](#)
- [47] Jing Zhang, Xin Yu, Aixuan Li, Peipei Song, Bowen Liu, and Yuchao Dai. Weakly-supervised salient object detection via scribble annotations. In *Proceedings of the IEEE/CVF conference on computer vision and pattern recognition*, pages 12546–12555, 2020. [3](#), [12](#), [13](#)
- [48] Jing Zhang, Tong Zhang, Yuchao Dai, Mehrtash Harandi, and Richard Hartley. Deep unsupervised saliency detection: A multiple noisy labeling perspective. In *Proceedings of the IEEE conference on computer vision and pattern recognition*, pages 9029–9038, 2018. [3](#), [6](#), [12](#), [13](#)
- [49] Weilin Zhang and Yu-Xiong Wang. Hallucination improves few-shot object detection. In *Proceedings of the IEEE/CVF Conference on Computer Vision and Pattern Recognition*, pages 13008–13017, 2021. [1](#)
- [50] Zhun Zhong, Liang Zheng, Guoliang Kang, Shaozi Li, and Yi Yang. Random erasing data augmentation. In *Proceedings*

of the AAAI conference on artificial intelligence, volume 34, pages 13001–13008, 2020. [5](#)

- [51] Wangjiang Zhu, Shuang Liang, Yichen Wei, and Jian Sun. Saliency optimization from robust background detection. In *Proceedings of the IEEE conference on computer vision and pattern recognition*, pages 2814–2821, 2014. [3](#), [12](#), [13](#)

From Saliency to DINO: Saliency-guided Vision Transformer for Few-shot Keypoint Detection (Supplementary Material)

Changsheng Lu¹, Hao Zhu¹, Piotr Koniusz^{2,1}

¹The Australian National University ²Data61/CSIRO

{ChangshengLuu, allenhaozhu}@gmail.com, Piotr.Koniusz@data61.csiro.au

A. Further Details for Approach

A.1. Visualizations of Various Saliency Priors

Fig. 7 shows examples of saliency maps produced by unsupervised (RBD [51], DINO [7], and MNL [48]), weakly-supervised (WScribble [47]), and supervised detectors (SCRN [42]). As one can see, saliency maps usually capture foreground objects. When the foreground and background have distinct colors and textures, both traditional and deep learning based detectors separate the salient objects well from backgrounds (top two rows, Fig. 7). If foreground and background are similar in color/texture, RBD may fail (third row, Fig. 7). We notice that MNL and DINO perform well despite they are entirely trained without the human-annotated labels.

A.2. Analysis of Saliency Detectors

Table 9 shows MNL enjoys very fast inference speed at 1.67 ms/img with 16.3M parameters. DINO is the fastest (0.03 ms/img) and has no extra parameters as its saliency is produced from the DINO backbone itself. Compared to other models listed in the table, MNL and DINO are very efficient in terms of the inference time (MNL and DINO are very fast) and the low number of parameters (generating saliency priors with DINO does not introduce extra parameters at all when DINO is used as the backbone). In our implementation, the saliency is pre-extracted once to facilitate easy training.

A.3. Architecture Details

Let (k, s, p) be the parameters of a convolution (conv.), where k is kernel size, s is stride, and p is padding.

Saliency Embedding Module (SEM) includes a large-

Table 9. Additional parameters and inference time (IT) of various saliency detectors.

Sal. Det.	RBD	WScribble	DINO	MNL	SCRN
Add. Params (M)	0	15.5	0	16.3	25.2
Add. IT (ms)	265.39	29.60	0.03	1.67	19.25

stride conv., three small-stride conv., and a 1×1 conv. Except the last 1×1 conv., each layer is followed by a ReLU to introduce non-linearity.

SalViT based Feature Encoder \mathcal{E} is comprised of a CNN or DINO backbone, one or multiple cascaded SalViTs, and a SEM which is shared by all SalViT blocks, where the backbone is used for extracting raw tokens \mathbf{F}^{raw} , whereas the SalViT blocks are used for learning relations among these raw tokens, with the focus on foreground patches under the guidance of saliency. The output of each SalViT block is passed through a layer normalization (LN) and a fully-connected layer (FC), and then all outputs are concatenated along the channel mode to form $\mathbf{F}^{\text{vit}} = [\mathbf{F}^1; \dots; \mathbf{F}^T]$, where $\mathbf{F}^t \in \mathbb{R}^{l \times l \times (d_{\text{vit}}/T)}$ and T is the number of SalViT blocks. Finally, \mathbf{F}^{raw} and \mathbf{F}^{vit} are combined to form the output $\mathcal{E}(\mathbf{I})$.

Descriptor Net, denoted by \mathcal{D} , contains dedicated 1×1 conv. layer to adjust feature channel and a series of conv. layers with $(k = 3, s = 2, p = 1)$ to reduce the resolution of the attentive feature maps down to desired sizes. Finally, the output feature map is flattened into a feature vector that serves as a descriptor.

B. Further Details for Experiment Setup

B.1. Implementation Details

Our Approach: The M-SA of our SalViT has 6 attention heads with each head using the linear projection to 64 dimensional space. The localization net \mathcal{G} uses three scales $S = \{8, 12, 16\}$. We use Adam as optimizer and set the learning rate to $1e-4$. Moreover, we set $W = 2$ and $\eta = 20$ by default in transductive FSKD.

ProtoNet: Original ProtoNet [33] forms the prototype for each class and classifies the query sample based on the nearest neighbor classifier (using the Euclidean distance). Similarly, we adapt ProtoNet to form support keypoint prototype (SKP) and compute the similarity between SKP and the feature vector at each position in query image. The location with the highest similarity is the detected keypoint.

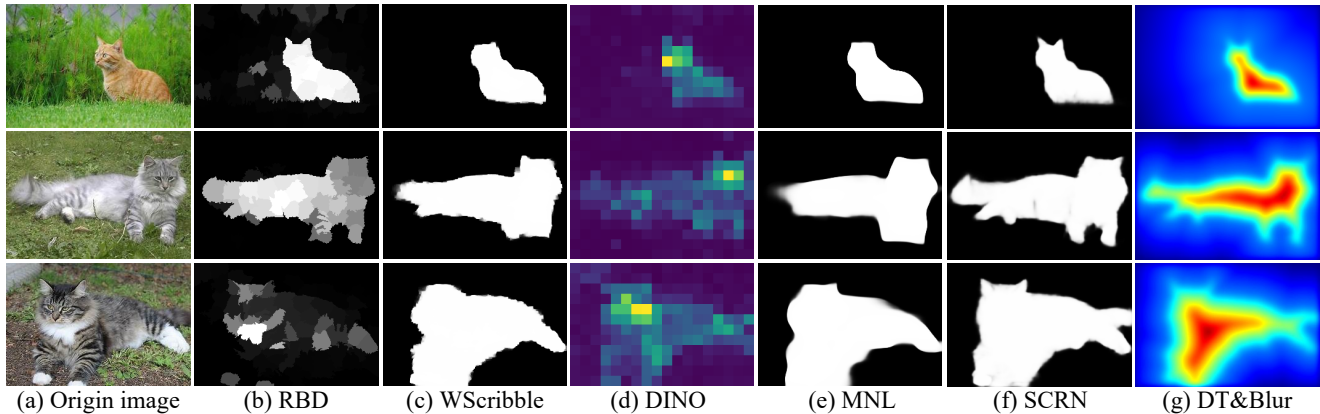


Figure 7. Examples of saliency prior masks generated by different models. The first column shows a selection of input images. Columns (b) to (f) show masks obtained with RBD [51], WScribble [47], DINO [7], MNL [48], and SCRNN [42]. The rightmost column shows the pre-processed saliency maps of column (f) after the distance transform (DT) and blur. The colored maps in the last column are for better visualization of saliency diffusion from foreground to background.

RelationNet: We expand each SKP (d -dimensional vector) to be the same size as the query feature map ($l \times l \times d$), and then concatenate the expanded SKP and query feature map to form a pair of features for *pixel-wise* relation learning using a relation module [34]. This approach is similar to FSS [26].

WG: Similar to [18, 16], we predict the weights of keypoint localization net by using the feature averaging based mechanism and the attention-based mechanism. The attention-based mechanism composes the parameters of novel keypoint detector by retrieving the parameters of base keypoint detector using attention (please see [18, 16] for more details). Thus, we can construct two approaches WG and WG (w/o Att.) for comparisons.

Experiment Protocol: All-way K -shot ($K = 1, 5$) protocol is used on all tasks. Specifically, each episode has K support images. All base (or novel) keypoints serve as support keypoints. The episode is formed from same-species images. The model is trained on seen species with base keypoints while tested on unseen species with novel keypoints. We also evaluate performance for base keypoints (where available) on unseen species using identically-trained model.

B.2. Keypoint Splits

1) **Animal pose dataset.** *Base keypoint set:* two ears, nose, four legs, four paws; *Novel keypoint set:* two eyes, four knees. 2) **AWA pose dataset.** *Base keypoint set:* two ear-bases, nose, neck base, neck end, throat base, throat end, tail, four legs, four paws, belly bottom, belly middle right, belly middle left; *Novel keypoint set:* two eyes, four knees. 3) **CUB.** *Base keypoint set:* beak, belly, back, breast, crown, two legs, nape, throat, tail; *Novel keypoint set:* forehead, two eyes, two wings. 4) **NABird.** *Base keypoint set:* beak,

Table 10. Study on the number of selected pseudo labels η in transductive FSKD. The harmonic scores of 1-shot keypoint detection are reported. “Q” with the number indicates the number of test query images.

Setting	Animal	AWA
<i>Inductive</i>	49.26	68.18
<i>Trans.</i> ($\eta = 06$, Q15)	50.08 (+0.82)	68.89 (+0.71)
<i>Trans.</i> ($\eta = 10$, Q30)	50.73 (+1.47)	69.13 (+0.95)
<i>Trans.</i> ($\eta = 15$, Q45)	51.39 (+2.13)	69.84 (+1.66)
<i>Trans.</i> ($\eta = 20$, Q60)	52.49 (+3.23)	70.79 (+2.61)

belly, back, breast, crown, nape, tail; *Novel keypoint set:* two eyes, two wings. 5) **DeepFashion2.** *Base keypoint set:* 158 total keypoints on 6 upper-body clothing categories; *Novel keypoint set:* 136 total keypoints on 7 lower-body clothing categories¹.

C. Additional Ablation Studies

Number of Pseudo Labels: Table 10 shows that increasing the number of selected pseudo labels yields better performance. Compared to the inductive inference, our model achieves improvements of 3.23% and 2.61% if selecting 20 pseudo labels out of 60 query images in Animal and AWA pose datasets, respectively. We also notice that increasing the number of pseudo labels will eventually make the performance saturated.

D. Further Results on FSKD Under Occlusion

Occlusion Visualization: The occlusion types regarding *gray box*, *average-pixel box*, and *background crop* are visualized in Fig. 8, which shows that the *background crop* (a

¹Please check <https://github.com/switchablenorms/DeepFashion2> for more details.

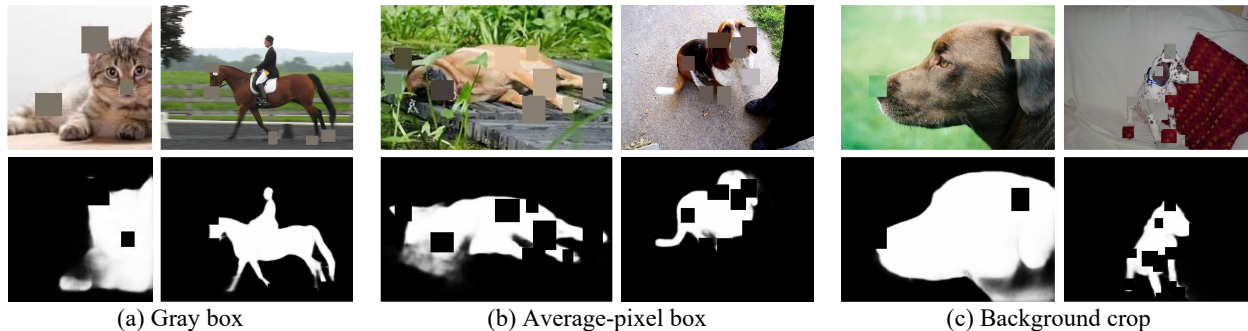


Figure 8. Visualization of three types of occlusions used in testing.



Figure 9. Examples of few-shot keypoint detection for unseen species under occlusions. Rows (a) and (b) are for detecting novel keypoints while (c) is for detecting base keypoints. The dashed boxes in red, yellow, and pink represents using occlusion types of *background crop*, *gray box*, and *average-pixel box*, respectively. Within each dashed box, the left-top image is the support, the left-bottom one is the query, and the right shows the detected keypoints with uncertainty.

Table 11. Testing results under occlusion of **gray box**. The model is trained using masks of *gray box* with various masking strategies. The average PCK scores of novel keypoint detection on *five* subproblems in Animal pose dataset are reported.

RGB	Sal.	Feat.	0%	30%	50%	100%
			45.40	37.33	32.46	20.08
✓			45.66	42.08	40.53	36.42
✓	✓		46.16	42.64	40.68	35.94
✓	✓	✓	45.81	42.06	40.16	34.53
	✓	✓	45.86	37.69	32.80	20.14

crop extracted from the background and transplanted into the foreground) is the best type of simulated occlusion. For example, the “nose” of the dog in Fig. 8(c) is realistically occluded.

Testing with Various Occlusions: The testing results under occlusion of *gray box* and occlusion of *average-pixel box* are shown in Tables 11 and 12, respectively. Compared to Table 7 which uses occlusions of *background crop* type

Table 12. Testing results under occlusion of **average-pixel box**. The model is trained using masks of *gray box* with various masking strategies. The average PCK scores of novel keypoint detection on *five* subproblems in Animal pose dataset are reported.

RGB	Sal.	Feat.	0%	30%	50%	100%
			45.16	38.34	34.06	22.60
✓			45.54	42.21	40.80	36.40
✓	✓		45.90	42.58	40.94	36.33
✓	✓	✓	45.94	42.40	40.41	35.35
	✓	✓	46.38	38.71	34.39	22.81

in the main paper, this experiment shows that the scores are higher if one uses *gray box* or *average-pixel box* as testing occlusions (e.g., when both RGB and saliency maps are masked, comparing 35.94% in Table 11 and 36.33% in Table 12 to 29.77% in Table 7), because *gray box* and *average-pixel box* are simpler and induce lesser domain shift compared with the training masks of *gray box*. Regardless of occlusion types, the FSKD with SalViT model equipped with

Table 13. Ablations of various masking and alignment (MAA) strategies under testing occlusion of **gray box**. The results are the average over five subproblems on the Animal pose dataset. Non-Occl means adding the prediction loss from non-occlude images. Y: applied; N: not applied.

Mask	Alignment	0%	50%	100%
N	N	45.40	32.46	20.08
Y	N	46.16	40.68	35.94
Y	SimMIM [44]	45.87	40.59	36.78
Y	Non-Occl Loss	46.20	40.16	36.14
Y	Feat. Align (MMD)	45.76	40.05	35.50
Y	Feat. Align (ℓ_2)	46.40	41.25	36.75
Y	Feat. Align (ℓ_1)	46.59	40.31	36.00
Y	Prob. Align	46.44	41.52	38.40

Table 14. Ablations of various masking and alignment (MAA) strategies under testing occlusion of **average-pixel box**. The results are the average over five subproblems on the Animal pose dataset. Non-Occl means adding the prediction loss from non-occlude images. Y: applied; N: not applied.

Mask	Alignment	0%	50%	100%
N	N	45.16	34.06	22.60
Y	N	45.90	40.94	36.33
Y	SimMIM [44]	45.82	41.21	37.02
Y	Non-Occl Loss	45.88	40.84	36.13
Y	Feat. Align (MMD)	45.24	40.16	35.70
Y	Feat. Align (ℓ_2)	46.01	40.77	37.14
Y	Feat. Align (ℓ_1)	46.20	40.93	36.25
Y	Prob. Align	46.29	42.24	38.54

our masking strategy outperforms regularly-trained model (*i.e.*, no masking applied) by a large margin, which validates that the masking strategy is useful and the image-masked model has learned to handle occlusions to some degree.

MAA Strategy: Firstly, we provide two baselines: i) the normally-trained model without masking input (*i.e.*, RGB + saliency) and without alignment; ii) the model trained with masking input but without the alignment strategy. Then, we investigate different alignment approaches to improve handling occlusions. SimMIM [44] recovers the raw pixel values of randomly masked image patches with a linear layer under the ℓ_1 loss, which can be regarded as alignment in the image space. Thus, we select SimMIM for comparisons. Since we have access to both occluded and non-occluded views of input, the prediction loss from non-occluded images can be added into the joint optimization, in addition to \mathcal{L}_{ms}^{occ} in Eq. 11 (in the main paper). The “Non-Occl Loss” and “Occl Loss” are forced to make the same predictions, thus one can think they implicitly perform alignment between two data views. Finally, we compare variants of feature alignment based on various distance metrics (ℓ_1 , ℓ_2 , and and MMD [2]), and probability alignment. From Tables 13 and 14, we observe: 1) Choosing which modality/signal to



Figure 10. Selected examples of failure cases for novel keypoint detection on unseen species. The dots refer to GT query keypoints. The tilted cross centered at an ellipse reflects the keypoint prediction with uncertainty. The line that connects GT and predicted keypoint reflects the localization error.

align is crucial. The probability alignment is very effective and outperforms other approaches; 2) Using SimMIM (alignment in the image space) and feature alignment are useful under severe occlusions of 100%. Feature alignment with the ℓ_1 or ℓ_2 metric is better than using the MMD metric; 3) The testing scores under occlusions of *gray box* (Table 13) and *average-pixel box* (Table 14), again, are higher than under occlusions of *background crop* (Table 8, in main paper). These results manifest that the simple MAA can improve occlusion handling in our FSKD with SalViT model. **Visualization Results:** Fig. 9 shows the visualization of few-shot keypoint detection under three types of occlusions. The query keypoint is randomly occluded with the probability of 0.3. As one can see, our model with simple MAA can effectively infer the locations of novel and base keypoints for unseen species, even though the body part is entirely occluded with visually realistic occlusions. Moreover, the estimated uncertainty (*i.e.*, blue ellipses in Fig. 9) still correlates well with the shape of body parts under occlusion setting.

E. Failure Cases and Future Work

Development of a keypoint learner that can efficiently detect arbitrary novel keypoints given a few exemplars remains an open question. Although our SalViT partially addresses FSKD by providing the informative relations within foreground patches for keypoint inference, FSKD can fail when colors and textures are indistinguishable. For example, the body part “knee” of the cat has been wrongly detected as “paw”, as shown in the first image of Fig. 10. Moreover, as FSKD is a very hard problem (arguably harder than standard FSL and FSOD), the keypoint predictions are usually imperfect (see localization error in Fig. 10). Although our modelled uncertainty mitigates this issue well, we hope to further improve the localization accuracy in our future works.